Experimental demonstration of splitting rules for exceptional points and their topological characterization

Yi-Xin Xiao [*,†] Jing Hu,[*] Zhao-Qing Zhang, and C. T. Chan[‡]
Department of Physics, Hong Kong University of Science and Technology, Clear Water Bay, Hong Kong, China

In non-Hermitian systems, the eigenvalues near exceptional points of order N (EPNs) usually exhibit $E \sim \Lambda^{1/N}$ dispersion/splitting under a small perturbation Λ. Such high sensitivity to perturbation makes them ideal candidates for sensors. However, $E \sim \Lambda^{1/m}$ dispersions with $m = 1, 2, \ldots, N-1$ are also possible for EPNs. Using a transposed Jordan block (TJB) matrix H_0 as a representative Hamiltonian, we present general rules that provide a unified understanding of the splitting behaviors of EPNs in diverse systems. Specifically, when the k-diagonal entries $(H_0)_{i,i+k}$ of H_0 are perturbed by Λ, we observe a dispersion of the form $E \sim \Lambda^{1/m}$, where $m = k + 1$. The phase rigidity's exponent χ and discriminant number ν together can serve as topological invariants to completely characterize an EPN with $E \sim \Lambda^{1/m}$ splitting, and they are proportional, i.e., $\chi = \nu/N = (N-1)/m$. The results are demonstrated experimentally using electrical circuits. Next, we demonstrate the applicability of the splitting rules to general non-TJB Hamiltonians that exhibit an EPN through an example. Moreover, we observe that the splitting of EPNs can lead to the emergence of lower-order EP structures, such as EP2 ellipses in the parameter space. We find that the EP2 ellipses exhibit two types of coalescence: with and without an increase in the EP order.

I. INTRODUCTION

It is crucial to understand the behavior of non-Hermitian (NH) Hamiltonians because they can effectively describe systems coupled to their environment. One prominent phenomenon in NH physics is the occurrence of exceptional points (EPs), which are degeneracies associated with the coalescence of eigenvectors [1–3]. Early research focused on EPs of order 2 (EP2s) [2–8], where two eigenvectors coalesce, while recent studies have investigated higher-order EPs [9–15]. The challenges in achieving higher-order EPs can be mitigated by the presence of certain symmetries [16–18]. Extensive research on EPs have inspired various applications such as lasing [19,20] and sensing [11,21].

Phase rigidity ρ, which describes eigenvectors' orthogonality properties, can be used to characterize EPN splitting, as it exhibits power-law behavior $\rho \sim \Lambda^\chi$ with different χ values for different energy dispersions near the EPN [22,23]. The Petermann factor, which underlies the increase in the intrinsic laser linewidth due to nonorthogonality of laser modes, can be expressed as the inverse square of phase rigidity [10]. EPs can also be characterized by the discriminant number [16,24] which is a topological invariant determined by the eigenvalue-based discriminant, besides other topological invariants like vorticity [25,26], Berry phase [27–29], winding number [30], knot invariant [31,32], and braid degree [33].

For degeneracies in Hermitian systems, perturbation-induced energy shift often scale linearly with perturbation strength. In contrast, a perturbation Λ applied to an EP of order N (EPN) typically results in a $E \sim \Lambda^{1/N}$ dispersion, implying an ultra-sensitive response which is ideal for sensor applications [11,21]. However, $E \sim \Lambda^{1/m}$ dispersions with $m < N$ near an EPN are also reported sometimes [11,14,15,18,22,25,29,34–39]. For example, a splitting exponent of 1/4 was observed near an EP6 in Ref. [14], and 1/2 was observed near an EP3 in Ref. [29]. An EP is termed anisotropic or hybrid if two different types of perturbations Λ, Ξ induce different dispersions, e.g., $E \sim \Lambda^{1/m}$ and $E \sim \Xi^{1/m'}$ with $m' \neq m$ [22,25]. A clear and unified understanding about when and why $E \sim \Lambda^{1/m}$ ($m \in \{1, \cdots, N\}$) occurs in various EPN systems is still lacking.

In this work, we establish an intuitive understanding of EPN splitting under perturbation by drawing a connection to the well-known NH skin effect, which denotes the localization of many bulk eigenstates at the boundary of certain NH systems [40–46]. Without loss of generality, we consider a representative EPN system whose Hamiltonian H_0 is a $N \times N$ transposed Jordan block (TJB) matrix and possesses NH skin effect, noting that the spectrum of a general EPN system can be related to H_0 by a similarity transformation. We find a correspondence between the splitting exponent $1/m$ in the dispersion relation $E \sim \Lambda^{1/m}$ and the k-diagonal entries $(H_0)_{i,i+k}$ that are perturbed: $m = k + 1$, where $k \in \{0, 1, \ldots, N\}$ is the range of the perturbative hopping Λ. We then establish general splitting rules for EPNs under various perturbation scenarios, which determines the energy dispersion and whether a lower-order EP (EPτ with $\tau < N$) may survive. The splitting rules provides a unified understanding of various dispersions near an EPN that could occur in diverse systems including PT-symmetric ones [11,15,18,29,36–39], e.g., $E \sim \epsilon^{1/4}$ near an EP6 in Ref. [14].

---

[*]These authors contributed equally to this work.
[†]Corresponding author: yxxiao@ust.hk
[‡]phchan@ust.hk

Furthermore, we show that an EPN exhibiting $E \sim \Lambda^{1/m}$ splitting can be fully characterized by using the phase rigidity exponent χ and discriminant number ν together as topological invariants, which individually are insufficient. We determine χ and ν from the eigenvectors and eigenvalues, respectively, and find that they are proportional with $\chi = \nu/N = (N-1)/m$. Moreover, we show that multiple EP2 curves can emanate from an EPN when we have two independent (perturbation) parameters that cause distinct splitting behaviors. An interesting example is a tridiagonal Hamiltonian that exhibits two types of splitting behaviors, namely $E \sim \delta_t^{1/2}$ and $E \sim \delta_\epsilon$ near an EPN. In this case, we reveal the existence of multiple EP2 ellipses touching at two EPNs, and identify two types of coalescence of EP2 ellipses: with and without an increase in the EP order.

In Sec. II, we establish the splitting rules of EPNs and show that an EPN exhibiting $E \sim \Lambda^{1/m}$ splitting can be topologically characterized by phase rigidity exponent χ and discriminant number ν together. In Sec. III, we experimentally demonstrate the splitting rules using electric circuits. In Sec. IV, we demonstrate the applicability of the splitting rules to general non-TJB Hamiltonians that possess an EPN through an example. In Sec. V, we show that, in a class of systems with two types of perturbations, multiple EP2 ellipses can emerge from two EPNs. Furthermore, we show that the EP2 ellipses can exhibit two types of coalescence: with and without an increase in EP order. We then conclude in Sec. VI.

II. RULES FOR EPN SPLITTING AND THEIR EXPERIMENTAL DEMONSTRATIONS

A. Understanding EP splitting via non-Hermitian skin effect

The Hatano-Nelson model [47] is a prototypical model embodying the NH skin effect [40–46,48]. If we parametrize the nonreciprocal hoppings t_1, t_2 ($t_1 \neq t_2$) in a Hatano-Nelson Hamiltonian H_{hn} with N sites as $t_{1,2} = t \mp 1$, then two EPNs occur at $t = \pm 1$. By taking $t = 1$, we obtain $H_{hn} = 2H_0$, where H_0 is a $N \times N$ TJB matrix that possesses an EPN. We have $(H_0)_{ij} = \delta_{i,j+1}$, $\forall i \in \{2, 3, \cdots N\}$. We note H_0 is representative of general systems that exhibit an EPN since they are related by similarity transformations. The value of N indicates both the EP order and the site number within H_0.

We examine how eigenvalues split in response to perturbations added to H_0. To start, we introduce a perturbative coupling $\Lambda \in \mathbb{C}$ ($|\Lambda| \ll 1$) to a 4-site chain H_0 (i.e., H_0 has dimensions of 4×4), as shown in Fig. 1(a), so that we have

$$H_a = H_0 + H'_a = \begin{pmatrix} 0 & 0 & 0 & \Lambda \\ 1 & 0 & 0 & 0 \\ 0 & 1 & 0 & 0 \\ 0 & 0 & 1 & 0 \end{pmatrix}. \quad (1)$$

That is, $(H'_a)_{ij} = \Lambda \delta_{i1} \delta_{j4}$. We note that subscripts "a," "b," etc., are used to distinguish between different example systems H that are obtained by perturbing H_0.

To facilitate our discussion, we define the k-diagonal of a $N \times N$ matrix A as the set of entries $(A_{i,i+k})$, namely the set of entries (A_{ij}) that satisfy $j - i = k$, $k = 1 - N, \ldots, N - 1$. For example, the diagonal and superdiagonal of a matrix correspond to $k = 0$ and $k = 1$, respectively. We can say that Λ
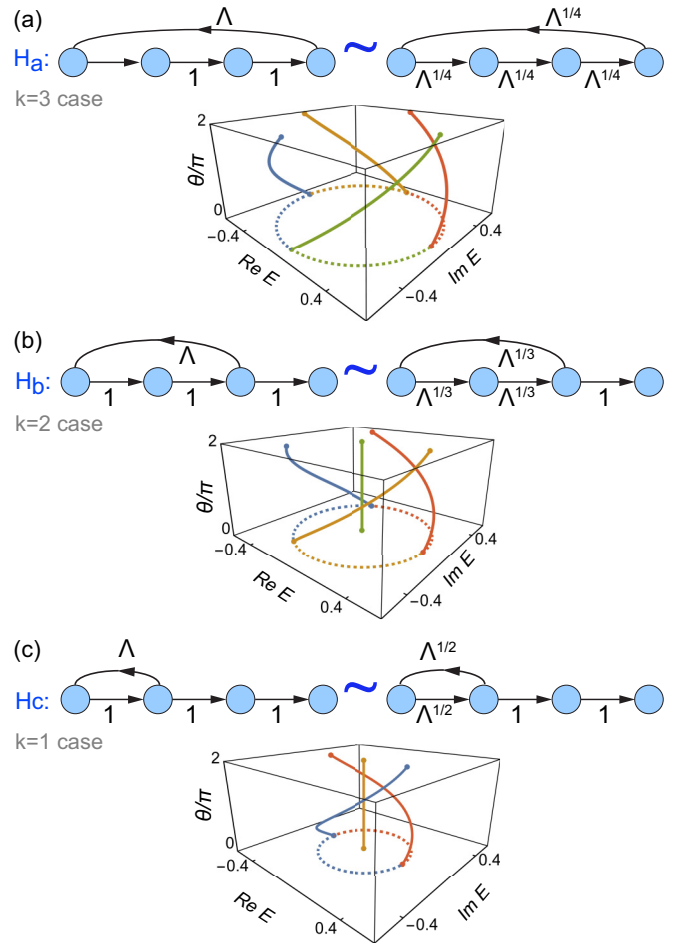
FIG. 1. [(a)–(c)] The systems H_a, H_b, H_c along with their spectrally equivalent systems, and the braids formed by their eigenvalue strands in the $(\text{Re}\,E, \text{Im}\,E, \theta)$ space, assuming $\Lambda = 0.1e^{i\theta}$. The arrows indicate the unidirectional hoppings. The symbol "$\sim$" represents similarity equivalence between two systems. The vertical line in panel (c) located at $E = 0$ is twofold degenerate.

appears in the 3-diagonal of H_a, implying the hopping range of $(H_a)_{14} = \Lambda$ is 3.

We observe that H_a has the same spectrum as that of a finite periodic chain [see Fig. 1(a)] represented by

$$\widetilde{H}_a = \Lambda^{1/4} \begin{pmatrix} 0 & 0 & 0 & 1 \\ 1 & 0 & 0 & 0 \\ 0 & 1 & 0 & 0 \\ 0 & 0 & 1 & 0 \end{pmatrix}, \quad (2)$$

which comprises uniform directional couplings $\Lambda^{1/4}$, noting that $S_1^{-1} H_a S_1 = \widetilde{H}_a$ with $S_1 = \text{diag}[\Lambda^{3/4}, \Lambda^{1/2}, \Lambda^{1/4}, 1]$. Then it is obvious that the eigenvalues of H_a scale as $E \sim \Lambda^{1/4}$, which is a manifestation of the NH skin effect—extreme sensitivity of the spectrum to changes in boundary conditions [40,41].

Figure 1(a) also depicts a four-strand braid formed by the eigenvalues of H_a in the $(\text{Re}\,E, \text{Im}\,E, \theta)$ space taking $\Lambda = 0.1e^{i\theta}$, which manifests the Riemann-surface topology of $\Lambda^{1/4}$. Projecting the strands onto the complex E plane yields dashed circles.

Likewise, with perturbation $(H_b)_{13} = \Lambda$ added to H_0, we have

$$
H_b = H_0 + H_b' = \left(
\begin{array}{ccc|c}
0 & 0 & \Lambda & 0 \\
1 & 0 & 0 & 0 \\
0 & 1 & 0 & 0 \\
\hline
0 & 0 & 1 & 0
\end{array}
\right),
$$

$$
\widetilde{H}_b = S_2^{-1} H_b S_2 = \left(
\begin{array}{ccc|c}
0 & 0 & \Lambda' & 0 \\
\Lambda' & 0 & 0 & 0 \\
0 & \Lambda' & 0 & 0 \\
\hline
0 & 0 & 1 & 0
\end{array}
\right),
\tag{3}
$$

as shown in Fig. 1(b), where $\Lambda' = \Lambda^{1/3}$ and $S_2 =$ diag$[\Lambda^{2/3}, \Lambda^{1/3}, 1, 1]$. The perturbation $(H_b)_{13} = \Lambda$ corresponds to a k-diagonal perturbation with $k = 2$. Inferring from $\widetilde{H}_b$, it is obvious that three eigenvalues of H_b split as $E \sim \Lambda^{1/3}$ and the fourth eigenvalue remains fixed at $E = 0$, as is embodied in the three-strand braid shown in Fig. 1(b).

In the third example shown in Fig. 1(c), the perturbation is applied to the 1-diagonal, i.e., $(H_c)_{12} = \Lambda$. Following previous reasoning, we find that two eigenvalues of H_c split as $E \sim \Lambda^{1/2}$, while the other two remain fixed at $E = 0$, yielding an EP2, as is shown in the two-strand braid in Fig. 1(c).

We observe that perturbations applied to the k-diagonal with $k = 3, 2, 1$ [as marked in Figs. 1(a)–1(c)] lead to splitting exponents of $1/m$ with $m = 4, 3, 2$, respectively. Our finding suggests that there is a relationship between the splitting exponent $1/m$ and the index k of the k-diagonal, namely, $m = k + 1$. Furthermore, it is possible that a remaining EP with lower order τ ($< N$) may exist after the splitting of the EPN.

B. General rules for EPN splitting

The results obtained from the motivating examples in Fig. 1 can be extended to a general $N \times N$ Hamiltonian $H = H_0 + H'$, yielding several general rules elaborated as (i)–(iii) below.

(i) When a single entry in the k-diagonal of H_0 is perturbed, i.e., $H_{ij}' = \Lambda \delta_{i, j-k}$ for $k \in \{0, 1, \ldots, N - 1\}$, then $m = k + 1$ eigenvalues split as $E \sim \Lambda^{1/m}$ and $\tau = N - m$ eigenvalues remain at $E = 0$. If $\tau \geqslant 2$, then an EPτ exists after the splitting of the EPN. We will show why the remaining τ-fold degeneracy after EPN splitting must be an EPτ instead of a nondefective degeneracy in Sec. II C.

The validity of (i) is illustrated by the three examples shown in Fig. 1 with $N = 4$ and $k = 3, 2, 1$, respectively. It is easily seen that the location of the single perturbed entry within a specified k-diagonal of H does not affect the splitting behavior.

(ii) When multiple entries in the k-diagonal of H_0 are perturbed, we can infer from (i) that the eigenvalues split as $E \sim \Lambda^{1/m}$ ($m = k + 1$). Compared to (i), the number of split eigenvalues may exceed m, noting that there can be at most N ($> m$) eigenvalues following $E \sim \Lambda^{1/m}$. Importantly, the split eigenvalues are enforced to form Q sets of m-tuples due to the Riemann-surface topology of $\Lambda^{1/m}$, where Q satisfies $Qm \leqslant N$ and $Q \in \mathbb{Z}^+$ and its value depends on the detailed perturbation. That is, when multiple entries in the k-diagonal are perturbed, Qm eigenvalues split as $E \sim \Lambda^{1/m}$ and $\tau = N - mQ$ eigenvalues remain at $E = 0$. An EPτ persists at $E = 0$ if $\tau \geqslant 2$. The value of Q can reach its maximum value,
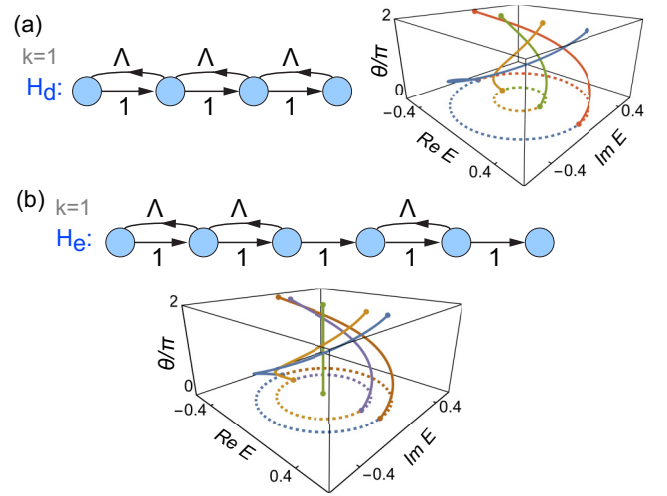
FIG. 2. (a), (b) The systems H_d, H_e and the braids formed by their eigenvalue strands in the $(\operatorname{Re} E, \operatorname{Im} E, \theta)$ space, assuming $\Lambda = 0.1 e^{i\theta}$. The arrows indicate the unidirectional hoppings. The vertical line in panel (b) located at $E = 0$ is twofold.

$Q_{max} = \lfloor N/m \rfloor$ ($\lfloor x \rfloor$ is the floor function), when the EPN is split to the utmost by perturbing all or enough entries in the k-diagonal [49]. The value of Q ranges from 1 to Q_{max}, depending on the specific perturbation applied to the k-diagonal.

Figure 2(a) shows an example system H_d with $N = 4$, which contains perturbation Λ at its all three 1-diagonal entries, causing $E \sim \Lambda^{1/m}$ with $m = 2$. This example has $Q = Q_{max} = \lfloor N/m \rfloor = 2$ and $\tau = N - Qm = 0$. In Fig. 2(a), we observe a pair of two-strand braids formed by the four eigenvalues of H_d. $Q = 2$ represents the number of braids, while $m = 2$ indicates the number of eigenvalues involved in each braid. We can also include different pre-coefficients to the Λ's without changing the $E \sim \Lambda^{1/m}$ splitting behavior.

Figure 2(b) shows an example system H_e with $N = 6$, in which only a subset of its eigenvalues split as $E \sim \Lambda^{1/2}$, when a perturbation Λ is applied to three of its 1-diagonals. In addition to a pair of two-strand braids formed by its four eigenvalues, we observe an EP2 that persists at $E = 0$. This example has $Q = 2$ and $\tau = N - Qm = 2$.

The braid structures in Figs. 2(a) and 2(b) imply that, for the general case when multiple entries in the k-diagonal of H_0 are perturbed, swapping occurs among each m-tuple, forming Q ($\in \{1, \ldots, Q_{max}\}$) sets of m-strand braids, as $\theta = \arg(\Lambda)$ accumulates 2π.

(iii) When multiple diagonals, e.g., k_1-, k_2-, ..., k_j-diagonal, are perturbed, the split eigenvalues follow $E \sim \Lambda^{1/m}$, where $m = \max\{k_1, \ldots, k_j\} + 1$, and Q and τ follow the same rule as in (ii).

An example system H_f is given in Fig. 3, where perturbation Λ appears at all entries in the 1-, 2-, and 3-diagonals of H_f and is denoted by blue arrows. The split eigenvalues are $E_{1,2} = \pm \Lambda^{1/4} + \Lambda^{1/2}/2 + O(\Lambda^{3/4})$ and $E_{3,4} = \pm i \Lambda^{1/4} - \Lambda^{1/2}/2 + O(\Lambda^{3/4})$, which all follow $E \sim \Lambda^{1/4}$ to the leading order, conforming to (iii). We observe a four-strand braid formed by E_1, E_2, E_3, and E_4 as shown in Fig. 3, assuming $\Lambda = 0.1 e^{i\theta}$.

We conclude that various splitting behaviors $E \sim \Lambda^{1/m}$, $m = 1, \ldots, N$ are possible for an EPN, depending on
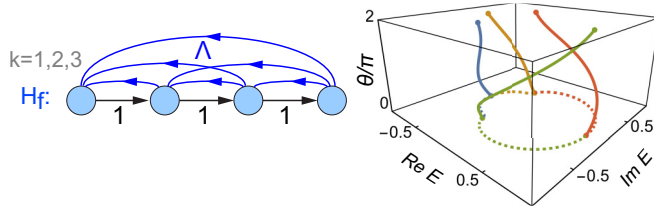
FIG. 3. The systems H_f and the braids formed by its eigenvalue strands in the $(\operatorname{Re}E, \operatorname{Im}E, \theta)$ space, assuming $\Lambda = 0.1e^{i\theta}$. The blue arrows represent the unidirectional hoppings Λ, which appear at all entries in the 1-, 2-, and 3-diagonals.

which k-diagonal the perturbation is applied to. The presented splitting rules offers a valuable tool to comprehend the diverse dispersions near an EPN in a wide range of systems, including PT-symmetric ones [11,14,15,18,29,36–39]. For example, the dispersion $E \sim \epsilon^{1/4}$ near an EP6 is demonstrated in Ref. [14]. We will show that $E \sim \epsilon^{1/4}$ results from the fact that, under a similarity transformation, the non-TJB Hamiltonian is equivalent to a TJB matrix H_0 with perturbation ϵ added to its 3-diagonal in Sec. IV. A carefully designed EPN-based sensor can achieve ultra-sensitivity of $\Delta E \sim \Lambda^{1/N}$ [11,14].

C. EPτ arising from EPN splitting

Following Sec. II B, we show why the remaining τ-fold degeneracy at $E = 0$ must be an EPτ, instead of a nondefective degeneracy.

For a matrix A, its null space (also known as kernel) is defined as $\ker(A) = \{\psi | A\psi = 0\}$. The nullity of A denotes the dimension of its null space and is represented by

$$\text{nullity}(A) = \dim[\ker(A)]. \tag{4}$$

The rank-nullity theorem [50] states that

$$\text{nullity}(A) = N_{\text{col}}(A) - \text{rank}(A), \tag{5}$$

where $N_{\text{col}}(A)$ is the number of columns in A.

For a general $N \times N$ TJB Hamiltonian H_0 that bears an EPN, its rank is obviously

$$\text{rank}(H_0) = N - 1. \tag{6}$$

For a Hamiltonian H that arises from adding perturbation to H_0, we must have

$$N - 1 \leqslant \text{rank}(H) \leqslant N, \tag{7}$$

which together with Eq. (5) leads to

$$0 \leqslant \text{nullity}(H) \leqslant 1. \tag{8}$$

We note that $\text{nullity}(H)$ reveals only the geometric multiplicity of $E = 0$ (i.e., count of eigenvectors associated with $E = 0$), but not its algebraic multiplicity. Equation (8) indicates that there is at most one eigenvector ψ_0 associated with $E = 0$. Therefore, it is guaranteed to have an EPτ when there are $\tau \geqslant 2$ eigenvalues remaining at $E = 0$.

D. Topological characterization

1. Phase rigidity exponent

Phase rigidity $\rho_n = |\langle \psi_n^L | \psi_n^R \rangle|$ of the nth state of H, which involves the normalized right and left eigenvectors, asymptotically takes the form $\rho_n \sim \Lambda^\chi$ near the EPN, where Λ is the deviation from the EPN [23,35]. We find that χ follows a universal rule: When the perturbation Λ is applied to the k-diagonal of H, i.e., when the split eigenvalues follow $E \sim \Lambda^{1/m}$, we have

$$\chi = (N - 1)/m, \tag{9}$$

where $m = k + 1$. Equation (9) arises from the fact that the eigenvectors take the following general form:

$$\langle \psi_n^L | \approx [1, A_1\widetilde{\Lambda}, \dots, A_{N-1}\widetilde{\Lambda}^{N-1}],$$
$$|\psi_n^R\rangle \approx [B_{N-1}\widetilde{\Lambda}^{N-1}, \dots, B_1\widetilde{\Lambda}, 1]^T, \tag{10}$$

where $\widetilde{\Lambda} = \Lambda^{1/m}$ with $|\Lambda| \ll 1$ and A_i, B_i are coefficients [49], and then

$$\rho_n = |\langle \psi_n^L | \psi_n^R \rangle| \sim \widetilde{\Lambda}^{N-1} = \Lambda^{(N-1)/m} \equiv \Lambda^\chi. \tag{11}$$

Obviously χ in Eq. (9) encodes the EP order N and the splitting exponent $1/m$.

2. Discriminant number

Degeneracies including EPs signify the vanishing of the discriminant $\mathcal{D}(X) = \prod_{i<j}[E_i(X) - E_j(X)]^2$ of the characteristic polynomial $f_E(X) = \det[E\mathbb{I} - H(X)]$, where X denotes the system parameters of $H(X)$ and E_i, E_j enumerate the eigenvalues.

We assume the EPN is split to the utmost (i.e., without remaining EPτ) by perturbations $c_1\Lambda, c_2\Lambda, \dots$ in the k-diagonal of H, where $\Lambda = \delta + i\zeta = |\Lambda|e^{i\theta}$ with $\delta, \zeta \in \mathbb{R}$. Taking $X = (\delta, \zeta)$, we have $\mathcal{D}(X_{\text{EP}}) = 0$ at the EPN $X_{\text{EP}} = (0, 0)$ on the $\delta\zeta$ plane. We introduce a topological invariant called discriminant number,

$$\nu = \frac{1}{2\pi i} \oint_\Gamma dX \cdot \nabla_X \ln \mathcal{D}(X), \tag{12}$$

to characterize the EPN, where Γ is any loop that encircles X_{EP} (i.e., the origin) in the $\delta\zeta$ plane [16,24].

We find that ν also follows a universal rule: For an EPN with splitting $\Delta E \sim \Lambda^{1/m}$ ($m = k + 1$) induced by a perturbation on the k-diagonal, we have

$$\nu = N(N - 1)/m = N\chi, \tag{13}$$

noting that $\mathcal{D} = \prod_{i<j}[E_i - E_j]^2 \sim (\Lambda^{1/m})^{N(N-1)}$. Since $\mathcal{D}(X)$ recovers itself after a cycle along Γ, ν must be an integer. Those (N, m) values that cause fractional ν as per Eq. (13) correspond to situations when ν is ill-defined due to the remnant EPτ on the $\delta\zeta$ plane [49].

The discriminant numbers of the EPNs exhibiting $E \sim \Lambda^{1/m}$ splitting are summarized in Table I, which follow Eq. (13). When there is a remaining EPτ, ν is not well-defined and applying Eq. (13) leads to an incorrect result, e.g., $\nu = 20/3$ is obtained when $(N, m) = (5, 3)$.

We note Eq. (13) reveals a correlation between the phase rigidity exponent χ derived from the eigenvectors and the discriminant number ν that is determined by the eigenvalues.

TABLE I. The discriminant numbers ν for different values of N (EP order) and m (inverse of splitting exponent). The discriminant number is not applicable for those entries with $m > N$ or for those corresponding to any remaining EPτ. Those entries are filled with the symbols "$/$" and "EPτ" ($\tau \geqslant 2$), respectively.

	$m=2$	3	4	5	6	7	8
$N=3$	3	2	$/$	$/$	$/$	$/$	$/$
$N=4$	6	4	3	$/$	$/$	$/$	$/$
$N=5$	10	EP2	5	4	$/$	$/$	$/$
$N=6$	15	10	EP2	6	5	$/$	$/$
$N=7$	21	14	EP3	EP2	7	6	$/$
$N=8$	28	EP2	14	EP3	EP2	8	7

They together provide a complete characterization of EPNs that exhibit $\sim \Lambda^{1/m}$ splitting, though individually, they are insufficient, for instance, $\nu = 10$ is obtained for both the cases of $(N, m) = (5, 2)$ and $(N, m) = (6, 3)$ and cannot distinguish between them.

III. EXPERIMENTAL IMPLEMENTATIONS AND DEMONSTRATIONS

A. Realization of a TJB Hamiltonian H_0

To experimentally observe the eigenvalue splitting and the phase rigidity exponent near an EP, we employ electric circuits to realize the model systems by mapping a Hamiltonian to a circuit Laplacian $\mathcal{L}$ that relates the input currents I and node voltages V in a circuit through the equation $I = \mathcal{L}V$, where I and V are column vectors [14,61–63].

First we implement the Hatano-Nelson model H_{hn} that contains 4 sites using the circuit in the right panel of Fig. 4(a). Specifically, current-inversion negative impedance converters (INICs) are used to achieve nonreciprocal hoppings $t_{1,2} = t \mp 1$ in the Hatano-Nelson model H_{hn}: For the INIC detailed in Fig. 4(a), a current that runs rightward (leftward) through an INIC experiences a negative (positive) capacitance $-C_2$ (C_2) [49]. By selecting appropriate values for $C_{10}, C_{20}, C_{30}, C_{40}$ in
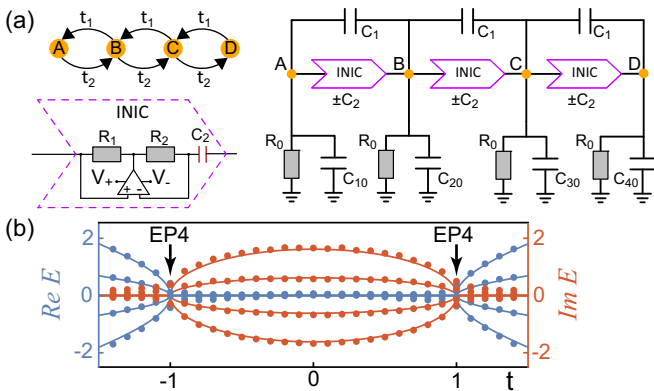
FIG. 4. (a) The circuit realization $\mathcal{L}_{hn}$ of the Hatano-Nelson model H_{hn} with nonreciprocal hoppings implemented by current-inversion negative impedance converters (INICs). (b) Experimental results (dots) for the occurrence of EP4s in the spectrum of $\mathcal{L}_{hn}$ in panel (a) agree well with results calculated from H_{hn} (lines).

Fig. 4(a), we can get a circuit Laplacian that takes a tridiagonal matrix form:

$$\mathcal{L} = y\mathbb{I} - i\omega \begin{pmatrix} 0 & C_- & 0 & 0 \\ C_+ & 0 & C_- & 0 \\ 0 & C_+ & 0 & C_- \\ 0 & 0 & C_+ & 0 \end{pmatrix}, \quad (14)$$

where $C_\pm = C_1 \pm C_2$ and $y = \frac{1}{R_0} + i\omega(C_{20} + 2C_1)$. If we assume $t = C_1/C_2$ such that $C_-/C_2 = t - 1 = t_1$ and $C_+/C_2 = t + 1 = t_2$, then we have

$$\mathcal{L}_{hn} = \frac{\mathcal{L} - y\mathbb{I}}{-i\omega C_2} = \begin{pmatrix} 0 & t_1 & 0 & 0 \\ t_2 & 0 & t_1 & 0 \\ 0 & t_2 & 0 & t_1 \\ 0 & 0 & t_2 & 0 \end{pmatrix}, \quad (15)$$

which has the same form as the Hatano-Nelson model H_{hn} with t_1 and t_2 appearing at the superdiagonal and subdiagonal, respectively. The parameter t can be tuned by adjusting the value of C_1 or/and C_2.

The matrix $\mathcal{L}$ can be obtained by measuring the voltage response at each node to input currents. Experimental details can be found in Ref. [49]. Using Eq. (15), we can then obtain the matrix $\mathcal{L}_{hn}$ and its corresponding eigenpairs. Figure 4(b) shows the variation of eigenvalues E with respect to t, featuring two EP4s at $t = \pm 1$. Errors are more noticeable around the EP4s due to their extreme sensitivity to experimental imperfection.

When $t = 1$, we realize the 4×4 TJB Hamiltonian H_0 noting that $\mathcal{L}_{hn}(t = 1) = 2H_0$. We observe $E \sim \sqrt{t - 1}$ near $t = 1$ in Fig. 4(b), since tuning t near $t = 1$ is effectively perturbing the 1-diagonal of H_0.

B. Experimental demonstrations of the splitting rules

By adding a small-valued capacitor C_Λ between nodes A and D as shown in Fig. 5(a) and selecting appropriate values for $C_{10}, C_{20}, C_{30}, C_{40}$, we realize

$$H_1 = \begin{pmatrix} 0 & 0 & 0 & \Lambda \\ 1 & 0 & 0 & 0 \\ 0 & 1 & 0 & 0 \\ \Lambda & 0 & 1 & 0 \end{pmatrix} \quad (16)$$

by $\mathcal{L}_1 = \frac{1}{-2i\omega C_2}(\mathcal{L} - y\mathbb{I})$ assuming $\Lambda = C_\Lambda/(2C_2)$, where $\mathcal{L}$ is the circuit Laplacian associated with Fig. 5(a) and $y = \frac{1}{R_0} + i\omega(C_{20} + 2C_1)$. Compared to H_a in Eq. (1), H_1 contains an extra Λ at $(H_1)_{41}$. It is worth noting that the presence of $(H_1)_{41} = \Lambda$ does not affect the eigenvalue splitting ($E \sim \Lambda^{1/4}$) and phase rigidity exponent to leading order, as can be easily verified. To avoid stability issues that arise from implementing H_a by connecting nodes "A" and "D" with an INIC, we opted to implement H_1 instead of H_a.

Similarly, we can realize

$$H_2 = \begin{pmatrix} 0 & 0 & \Lambda & 0 \\ 1 & 0 & 0 & \Lambda \\ \Lambda & 1 & 0 & 0 \\ 0 & \Lambda & 1 & 0 \end{pmatrix}, \quad (17)$$

by $\mathcal{L}_2 = \frac{1}{-2i\omega C_2}(\mathcal{L} - y\mathbb{I})$ assuming $\Lambda = C_\Lambda/(2C_2)$, where $\mathcal{L}$ is the circuit Laplacian associated with Fig. 5(b) which contains
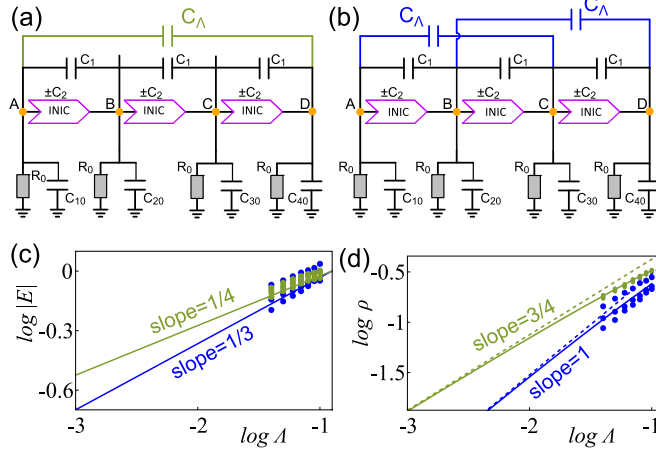
FIG. 5. (a), (b) The circuit realization of the 4×4 perturbed TJB Hamiltonians H_1 [Eq. (16)] and H_2 [Eq. (17)] by $\mathcal{L}_1$ and $\mathcal{L}_2$, where perturbation Λ is implemented by a capacitor C_Λ. (c) Energy splitting near the EP4 in the experimentally obtained $\mathcal{L}_1$ and $\mathcal{L}_2$ are denoted by green and blue dots, respectively. Theoretical results for H_1 and H_2 are denoted by lines. (d) Phase rigidities near the EP4 for $\mathcal{L}_1$, H_1 (green) and $\mathcal{L}_2$, H_2 (blue). Experimental and theoretical results are denoted by dots and lines, respectively. Dashed lines show the slopes in the small Λ limit, i.e., they are leading-order approximations of the solid lines. The spreading of dots reflects the extreme sensitivity of EP4 to experimental imperfection.

a small-valued capacitor C_Λ between nodes A and C, as well as between B and D. The extra terms $(H_2)_{31} = (H_2)_{42} = \Lambda$ do not affect the eigenvalue splitting and phase rigidity exponent to leading order.

In Fig. 5(c), the eigenvalues E are plotted against Λ for $\mathcal{L}_1$ and $\mathcal{L}_2$ obtained from experimental measurements. The green and blue dots represent the results for $\mathcal{L}_1$ and $\mathcal{L}_2$, respectively, which are consistent with the theoretical results (lines) that are obtained from H_1 and H_2 and follow $E \sim \Lambda^{1/4}$ and $E \sim \Lambda^{1/3}$. Since the four eigenstates coincide in $|E|$, we only observe one line for each case in Fig. 5(c).

The spreading of dots in Fig. 5(c), especially the blue dots for $\mathcal{L}_2$, arise from the extreme sensitivity near the EP4 to undesirable experimental artifacts such as the parasitic resistances of the capacitors. To mitigate the influence of experimental artifacts, experimental measurements were carried out using moderately small Λ values instead of very small ones, ensuring that Λ dominates over the artifacts.

Accordingly, the phase rigidity is plotted against Λ in Fig. 5(d) for the measured $\mathcal{L}_1$ and $\mathcal{L}_2$. The green and blue dots represent the results from measured $\mathcal{L}_1$ and $\mathcal{L}_2$, while the solid lines denote the results calculated from H_1 and H_2. For both H_1 and H_2, the phase rigidities of the four eigenstates are the same and represented by the same solid line in Fig. 5(d). The dashed lines with slopes of 3/4 and 1 represent the leading-order approximations of the solid lines in the limit of small Λ. And the slopes represent the phase rigidity exponents $\chi = 3/4$ and $\chi = 1$ for the eigenstates of H_1 and H_2, which obey the relation $\chi = (N-1)/m$ in Eq. (9). The experimental results (dots) agree with the theoretical results (lines), with some imperfection arising from the extreme sensitivity near the EP4 to undesirable experimental artifacts.

IV. APPLICABILITY OF THE SPLITTING RULE TO GENERAL EP*N* SYSTEMS

As previously noted, the Hamiltonian H_0 of TJB matrix form is representative of general systems $\mathcal{H}_0$ that exhibit an EP*N*. In the following, we will explain why and how the splitting rule applies to a general system $\mathcal{H}_0$ of dimensions $N \times N$ when subjected to perturbation.

Clearly, a similarity transformation $H_0 = S^{-1}\mathcal{H}_0 S$ can be used to relate $\mathcal{H}_0$ to a TJB matrix H_0, where S can be obtained through simple standard procedures. Using this transformation, the perturbed Hamiltonian $\mathcal{H} = \mathcal{H}_0 + \Delta\mathcal{H}$ can be transformed to a perturbed TJB matrix given by

$$H = S^{-1}\mathcal{H}S = H_0 + \Delta H, \qquad (18)$$

where $\Delta H = S^{-1}\Delta\mathcal{H}S$.

Equation (18) suggests that the rules (i)–(iii) for the EP*N* splitting apply to $\mathcal{H}_0$, but in an indirect way that we consider the effect of adding ΔH to H_0 instead. That is, the splitting exponent $1/m$ can be determined by inspecting which k-diagonal entries of H_0 in Eq. (18) are perturbed by ΔH.

For illustration, we show an example of non-TJB Hamiltonian that exhibits $E \sim \epsilon^{1/4}$ near an EP6 in a work about EP-based sensor, where ϵ is a perturbation parameter [14]. The Hamiltonian has the following form:

$$\mathcal{H} = \begin{pmatrix} 0 & 0 & 0 & i & 0 & 0 \\ 0 & 0 & 0 & 0 & i & 0 \\ 0 & 0 & 0 & 0 & 0 & i \\ -i & i & 0 & -i\gamma & 0 & 0 \\ i\mu & -2i\mu & i\mu & 0 & 0 & 0 \\ 0 & i & -i & 0 & 0 & i\gamma \end{pmatrix}, \qquad (19)$$

where $\gamma = (\sqrt{5}+1)/2$ is assumed. The EP6 occurs when $\mu = \mu_{EP} = (\sqrt{5}-1)/4$. The occurrence of the EP6 implies that we can find a similarity transformation $S^{-1}\mathcal{H}_0 S = H_0$ such that H_0 is a TJB matrix, where $\mathcal{H}_0 = \mathcal{H}(\mu_{EP})$. Explicitly we have

$$S = \begin{pmatrix} 1 & ic_1 & -c_2 & -ic_2 & c_1 & 0 \\ 1 & ic_1/2 & -1 & 0 & 0 & 0 \\ 1 & 0 & 0 & 0 & 0 & 0 \\ 0 & -i & c_1 & ic_2 & -c_2 & -ic_1 \\ 0 & -i & c_1/2 & i & 0 & 0 \\ 0 & -i & 0 & 0 & 0 & 0 \end{pmatrix},$$

where $c_1 = \sqrt{5}+1$ and $c_2 = \sqrt{5}+3$. The perturbation is introduced via $\mu = \mu_{EP}(1+\epsilon)$. In the presence of perturbation, we have

$$H = S^{-1}\mathcal{H}S$$

$$= \begin{pmatrix} 0 & 0 & 0 & 0 & 0 & 0 \\ 1 & 0 & 0 & 0 & 0 & 0 \\ 0 & 1 & 0 & -\epsilon & -ic_1\epsilon/2 & \epsilon \\ 0 & 0 & 1 & -i(c_1+c_2)\epsilon/c_2 & c_2\epsilon/2 & ic_1\epsilon/2 \\ 0 & 0 & 0 & 1+\epsilon & ic_1\epsilon/2 & -\epsilon \\ 0 & 0 & 0 & 0 & 1 & 0 \end{pmatrix}.$$

$$(20)$$

Obviously, H in Eq. (20) can be viewed as a perturbed TJB matrix with the perturbation parameter ϵ appearing in several

entries. According to the EPN splitting rule (iii) in Sec. II B, the perturbation $H_{36} = \epsilon$ that appears in the 3-diagonal of H dominates [compared to other ϵ's in Eq. (20)] and causes $E \sim \epsilon^{1/4}$ dispersion for $|\epsilon| \ll 1$.

The rule for phase rigidity, i.e, Eq. (9), also remains true for $\mathcal{H}$. We can understand it by looking at the definition of phase rigidity. The left eigenvector $\langle \psi_n' |$ and right eigenvector $\psi_n' \rangle$ of $\mathcal{H}$ are related to those of H via

$$\langle \psi_n' | = \langle \psi_n | S^{-1}, \qquad |\psi_n'\rangle = S|\psi_n\rangle. \tag{21}$$

The phase rigidity for an eigenstate of $\mathcal{H}$ is then

$$\rho_n' = |\langle \psi_n' | \psi_n' \rangle| = |\langle \psi_n | \psi_n \rangle| = \rho_n. \tag{22}$$

That is, the phase rigidities for eigenstates of $\mathcal{H}$ are the same as those for H.

The rule for discriminant number ν obviously holds for non-TJB form Hamiltonians, since the discriminant $\mathcal{D}$ only depends on the eigenvalues which are identical for $\mathcal{H}$ and H.

Furthermore, any $N' \times N'$ ($N' > N$) Hamiltonian exhibiting an EPN can be decoupled to obtain a $N \times N$ subsystem associated with the EPN.

V. EPNS SPLITTING INTO EP2 ELLIPSES

A. Emergence of EP2 ellipses

Next, we go beyond the energy dispersions in the vicinity of EPNs and investigate EPN splitting from a global perspective in the parameter space. We will see that EP2 curves can emerge from EPNs, which manifests the splitting of an EPN into lower-order EP curves. Generally when two perturbation parameters, e.g., $\Lambda, X \in \mathbb{R}$, are applied to different k-diagonals of H_0, EP curves emanate from the EPN in the ΛX plane, since there are two free parameters in the single constraint $\mathcal{D}(\Lambda, X) = 0$ noting $\mathcal{D} \in \mathbb{R}$.

An interesting system is the generalized Hatano-Nelson model below,

$$H_{\mathrm{dis}} = \begin{pmatrix} c_1\epsilon & a_1t_1 & 0 & 0 \\ b_1t_2 & c_2\epsilon & a_2t_1 & 0 \\ 0 & b_2t_2 & c_3\epsilon & \cdots \\ 0 & 0 & \cdots & \cdots \end{pmatrix}, \tag{23}$$

with arbitrary coupling coefficients (randomly chosen $a_i, b_i > 0$) and onsite energies (random $c_i \in \mathbb{R}$), $t_{1,2} = t \mp 1$ and $t, \epsilon \in \mathbb{R}$. Two EP$N$s occur at $(t, \epsilon) = (\pm 1, 0)$, where H_{dis} is similar to a $N \times N$ TJB matrix H_0 [49]. A deviation δ_t (δ_ϵ) from the EPN $(t, \epsilon) = (1, 0)$ is equivalent to a perturbation in the 1-diagonal (diagonal) of H_0 [49], inducing $\Delta E \sim \delta_t^{1/2}$ ($\Delta E \sim \delta_\epsilon$) and $\rho \sim \delta_t^{(N-1)/2}$ ($\rho \sim \delta_\epsilon^{N-1}$). EP curves are expected to emanate from the EPNs in the $t\epsilon$ plane.

For $f_E = \det(E\mathbb{I} - H_{\mathrm{dis}})$, the discriminant has the form

$$\mathcal{D}(t, \epsilon) = \sum_{j=0}^{M} B_j (\epsilon^2)^j (t_1t_2)^{M-j}, \tag{24}$$

where $M = \frac{N(N-1)}{2}$ and $B_j = B_j(a_i, b_i, c_i)$ are real coefficients [49]. Due to the realness of H_{dis}, its eigenvalues are either real or come in complex-conjugate pairs, causing $\mathcal{D}(t, \epsilon) \in \mathbb{R}$, which can also be argued from the perspective of pseudo-Hermiticity symmetry in H_{dis}, i.e., $\eta^{-1} H_{\mathrm{dis}} \eta = H_{\mathrm{dis}}^\dagger$ [17,49].
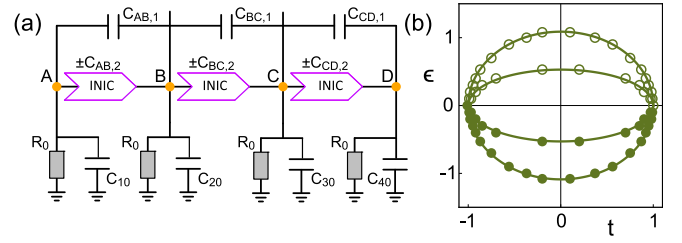
FIG. 6. (a) Circuit realization of a 4×4 system $H_{\mathrm{dis}}^{(1)}$ with $\{a_1, a_2, a_3\} = \{b_1, b_2, b_3\} = \{0.6, 0.4, 1.2\}$ and $\{c_1, c_2, c_3, c_4\} = \{3, 1, 2.8, 0.2\}$. (b) Experimentally measured EP2 ellipses (dots) from the circuit realization in panel (a).

Solving $\mathcal{D}(t, \epsilon) = 0$ gives us

$$t^2 + \epsilon^2/\alpha_j = 1, \qquad j = 1, \cdots, M, \tag{25}$$

Equation (25) represents a maximum of $n_{\max} = M$ EP2 ellipses in the $t\epsilon$ plane if $\alpha_j > 0$ for any $j \in \{1, \cdots, M\}$, which is possible for appropriate coefficients a_i, b_i, c_i in Eq. (23). An example will be illustrated shortly in Sec. V B.

When $t \in (-1, 1)$ and $\epsilon = 0$, H_{dis} is similar to an anti-Hermitian matrix and has eigenvalues in the form of $\pm iE_j$, $j = 1, 2, \ldots, \lfloor N/2 \rfloor$, where $\lfloor x \rfloor$ is the floor function [49]. When $\epsilon \to \pm \infty$, H_{dis} turns Hermitian and has real eigenvalues. Thus, there are at least $n_{\min} = \lfloor N/2 \rfloor$ EP transitions for any $t \in (-1, 1)$ as ϵ varies from 0 toward $\pm \infty$, which implies the existence of a minimum of $n_{\min} = \lfloor N/2 \rfloor$ EP2 ellipses in the $t\epsilon$ plane. The region outside the outermost EP2 ellipse is the exact phase with purely real eigenvalues.

For illustration, a 4×4 example of Eq. (23) with $\{a_1, a_2, a_3\} = \{b_1, b_2, b_3\} = \{0.6, 0.4, 1.2\}$ and $\{c_1, c_2, c_3, c_4\} = \{3, 1, 2.8, 0.2\}$, which we denote as $H_{\mathrm{dis}}^{(1)}$, is implemented using the circuit shown in Fig. 6(a). The parameters t and ϵ in $H_{\mathrm{dis}}^{(1)}$ can be tuned by judiciously choosing appropriate capacitors in Fig. 6(a).

The EP locations in the $\epsilon < 0$ half-plane are obtained from experimental measurements and shown as dots in Fig. 6(b), and their mirror images in the $\epsilon > 0$ half-plane are denoted by circles. Each EP dot is extracted from a measured $E(t)$ band diagram like the one shown in Fig. 4(b). Obviously the experimental results agree well with the ellipses solved from $\mathcal{D}(t, \epsilon) = 0$.

In the following, we show that the EP2 ellipses can exhibit two types of coalescence: with and without an increase in the EP order.

B. EP2 ellipses merging into an EP2 ellipse

Figure 7(a) shows that, in a 3×3 system $H_{\mathrm{dis}}^{(2)}$, the number of EP2 ellipses reduces from three (green) to two (blue dashed) and then to one (red), as c_3 is decreased from 9.2 to 9 and then to 8.8, fixing $\{a_1, a_2\} = \{1, 2\}$, $\{b_1, b_2\} = \{2, 5\}$ and $\{c_1, c_2\} = \{3, 4\}$. Specifically, the outer two green ellipses merge into one blue EP2 ellipse at $c_3 = 9$ (indicated by arrows), and then vanish as c_3 reduces further, which is also depicted by the Re $E(\epsilon)$ bands (with $t = 0$ fixed) in the inset of Fig. 7(a): Two EPs merge into one EP and then get gapped.

We note that the EP order does not increase when two EP2 ellipses coalesce at $c_3 = 9$. And there are as many as three
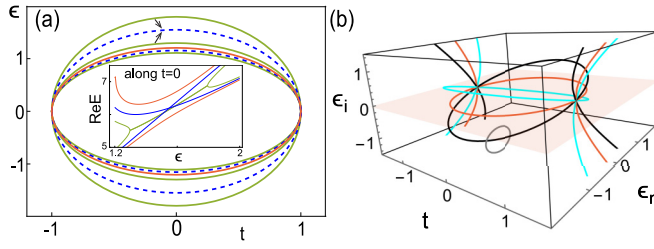
FIG. 7. (a) Three green, two blue, one red EP2 ellipses obtained for $c_3 = 9.2, 9$, and 8.8 in a 3×3 system $H_{\mathrm{dis}}^{(2)}$. Other coefficients are $\{a_1, a_2\} = \{1, 2\}$, $\{b_1, b_2\} = \{2, 5\}$, $\{c_1, c_2\} = \{3, 4\}$. Inset: two EP2s (green curves) merge into a single EP2 (blue curves), which disappears when a gap opens (red curves). (b) The EP3 nexus formed by ellipses and hyperbolas in $(t, \epsilon_r, \epsilon_i)$ space with $c_3 = 8$. Other coefficients are the same as in (a).

EP2 ellipses at $c_3 = 9.2$ as shown in Fig. 7(a), which represents a scenario where the maximum number of $n_{\mathrm{max}} = 3$ EP2 ellipses is achieved for $N = 3$.

Relaxing $\epsilon \in \mathbb{R}$ to $\epsilon \in \mathbb{C}$ and assuming $\epsilon = \epsilon_r + i\epsilon_i$, we have three degrees of freedom t, ϵ_r and ϵ_i for the two constraint equations, $\mathrm{Re}\,\mathcal{D} = 0$ and $\mathrm{Im}\,\mathcal{D} = 0$. Therefore we are guaranteed to have EP curves in the $(t, \epsilon_r, \epsilon_i)$ space. Actually we find there are always $M = \frac{N(N-1)}{2}$ EP2 ellipses in the $(t, \epsilon_r, \epsilon_i)$ space, noting that the derivation of Eq. (25) does not require ϵ to be real.

For example, Fig. 7(b) shows the EP2 ellipses in the $(t, \epsilon_r, \epsilon_i)$ space for the case of $c_3 = 8$, where the other coefficients are the same as in Fig. 7(a). Figure 7(b) is representative of $c_3 < 9$ cases including the $c_3 = 8.8$ case in Fig. 7(a). It turns out that two ellipses for $c_3 = 8.8$ in Fig. 7(a) are tilted away from the $t\epsilon_r$ plane, similar to the cyan and black ellipses in Fig. 7(b). Each EP2 ellipse is perpendicular to its corresponding EP2 hyperbola in the region of $|t| > 1$, and they share the same equation $t^2 + \epsilon^2/\alpha_j = 1$ [49]. Thus, the two EP3s at $(t, \epsilon_r, \epsilon_i) = (\pm 1, 0, 0)$ manifest as the chain points in the EP nexus formed by ellipses and hyperbolas.

Looping around any EP2 arc, as indicated by the gray circle in Fig. 7(b), yields a discriminant number of $\nu = 1$. Six EP2 arcs together give $\nu = 6$ at the EP3, conforming to Eq. (13) with $(N, m) = (3, 1)$. The EP nexus are topologically robust against smooth changes of the coefficients a_i, b_i, c_i in H_{dis}.

C. EP2 ellipses merging into an EP4 ellipse

EP2 ellipses can also coalesce in a different way to form a high-order EP ellipse, e.g., two EP2 ellipses can merge into an EP4 ellipse.

We consider $H_{\mathrm{dis}}^{(3)} = ts_x - is_y + \epsilon s_z$ with s_i being spin-3/2 matrices [60], which amounts to a 4×4 H_{dis} in Eq. (23) with $\{a_1, a_2, a_3\} = \{b_1, b_2, b_3\} = \{\frac{\sqrt{3}}{2}, 1, \frac{\sqrt{3}}{2}\}$ and $\{c_1, c_2, c_3, c_4\} = \{\frac{3}{2}, \frac{1}{2}, -\frac{1}{2}, -\frac{3}{2}\}$. Increasing c_4 from -1.7 to -1.3, we observe two EP2 ellipses (green) merging into one EP4 ellipse (blue dashed) when $c_4 = -3/2$ and then split into two EP2 ellipses (red), as is shown in Fig. 8(a). For illustration of the process of coalescence, we fix $t = 0$ and show the band structures $E(\epsilon)$ in Figs. 8(b)–8(d), where the real (imaginary) parts are represented by solid (dashed) curves, respectively.
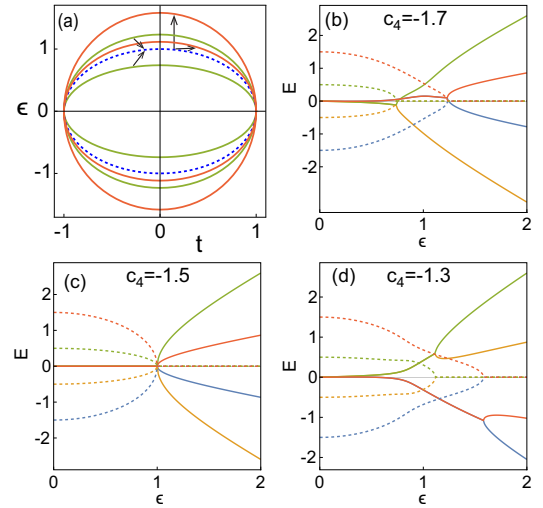
FIG. 8. (a) The occurrence of two EP2 ellipses (green), one EP4 ellipse (blue dashed), and two EP2 ellipses (red) in the $t\epsilon$ plane for $c_4 = -1.7, -1.5, -1.3$, respectively, in a 4×4 system $H_{\mathrm{dis}}^{(3)}$ with $\{a_1, a_2, a_3\} = \{b_1, b_2, b_3\} = \{\frac{\sqrt{3}}{2}, 1, \frac{\sqrt{3}}{2}\}$ and $\{c_1, c_2, c_3, c_4\} = \{\frac{3}{2}, \frac{1}{2}, -\frac{1}{2}, -\frac{3}{2}\}$. (b)–(d) Band structures $E(\epsilon)$ of the three cases in panel (a), where $t = 0$ is fixed. The real (imaginary) parts are denoted by solid (dashed) curves.

The merging of the two EP2 ellipses shown in Fig. 8(a) is different from that is shown in Fig. 7(a). The coalescence in Fig. 8(a) involves all 4 eigenstates and the induced EP4 ellipse constitutes a sixfold root of $\mathcal{D}$ in Eq. (24) [49], and the number of EP2 ellipses in the $t\epsilon$ plane is $n_{\mathrm{min}} = 2$, both before and after the coalescence. Compared to EP2 ellipses, the EP4 ellipse is fragile against tuning parameters since it necessitates stricter conditions.

VI. CONCLUSION

We formulated general rules that enable a unified description and understanding of EPN's splitting behaviors $E \sim \Lambda^{1/m}$, $m \in \{1, 2, \ldots, N\}$ in diverse systems. We found that the splitting exponent $1/m$ is determined by $m = k + 1$, where k represents the k-diagonal of the TJB matrix that is perturbed. The key in establishing the splitting rules is that every m eigenvalues form a group and split together in the form of $E \sim \Lambda^{1/m}$ when perturbed in the k-diagonal, and there can be an integer number of such groups. The EPN splitting behaviors observed in general systems on different platforms, such as photonics and phononics, can all be incorporated into the same framework simply by employing similarity transformations that map them to a TJB form. The rules for EPN splitting are demonstrated experimentally using electric circuits, which simulate Hamiltonians through circuit Laplacians. Our work can serve as a useful guide for optimizing the performance in EP-based sensors, by exploiting the $E \sim \Lambda^{1/N}$ response of the EPN to small variations in certain system parameters, instead of $E \sim \Lambda^{1/m}$ with $m < N$.

We use the phase rigidity exponent χ and discriminant number ν together as topological invariants to fully characterize any EPNs with any $\Lambda^{1/m}$ splitting behavior. We find that the two quantities χ and ν, determined from eigenvectors and

eigenvalues, respectively, are related by $\nu = N\chi$, since both the perturbed eigenvectors and eigenvalues contain the $\Lambda^{1/m}$ factor. Interestingly, when ν is ill-defined due to the remaining lower-order EP under perturbation, a meaningless fractional value is obtained from $\nu = N(N-1)/m$ [i.e., Eq. (13)]. This justifies the effectiveness of the discriminant number in an opposite perspective.

We then show that the EPN can split into EP2 curves when multiple parameters are allowed to vary. For example, in a generalized Hatano-Nelson model, we show the splitting of two EPNs into EP2 ellipses in the plane spanned by two parameters which individually induce square-root and linear dispersions near EPNs. The EP2 ellipses are found to exhibit two types of coalescence: with and without an increase in the EP order. This suggests that the splitting of a higher-order EP can lead to various EP geometries and complex evolution behaviors. This opens up a promising subfield for exploration and potential connections with other fields such as catastrophe theory and topology in physics.

[1] T. Kato, *Perturbation Theory for Linear Operators* (Springer-Verlag, Berlin, 1995).

[2] C. Dembowski, H.-D. Gräf, H. L. Harney, A. Heine, W. D. Heiss, H. Rehfeld, and A. Richter, Experimental Observation of the Topological Structure of Exceptional Points, Phys. Rev. Lett. **86**, 787 (2001).

[3] M. V. Berry, Physics of non-Hermitian degeneracies, Czech. J. Phys. **54**, 1039 (2004).

[4] W. D. Heiss, The physics of exceptional points, J. Phys. A: Math. Theor. **45**, 444016 (2012).

[5] C. M. Bender and S. Boettcher, Real Spectra in Non-Hermitian Hamiltonians Having PT Symmetry, Phys. Rev. Lett. **80**, 5243 (1998).

[6] S. K. Ozdemir, S. Rotter, F. Nori, and L. Yang, Parity-Time Symmetry and Exceptional Points in Photonics, Nat. Mater. **18**, 783 (2019).

[7] L. Xiao, T. Deng, K. Wang, Z. Wang, W. Yi, and P. Xue, Observation of Non-Bloch Parity-Time Symmetry and Exceptional Points, Phys. Rev. Lett. **126**, 230402 (2021).

[8] R. El-Ganainy, K. G. Makris, M. Khajavikhan, Z. H. Musslimani, S. Rotter, and D. N. Christodoulides, Non-Hermitian physics and PT symmetry, Nature Phys **14**, 11 (2018).

[9] K. Ding, Z. Q. Zhang, and C. T. Chan, Coalescence of exceptional points and phase diagrams for one-dimensional PT-symmetric photonic crystals, Phys. Rev. B **92**, 235310 (2015).

[10] Z. Lin, A. Pick, M. Lončar, and A. W. Rodriguez, Enhanced Spontaneous Emission at Third-Order Dirac Exceptional Points in Inverse-Designed Photonic Crystals, Phys. Rev. Lett. **117**, 107402 (2016).

[11] H. Hodaei, A. U. Hassan, S. Wittek, H. Garcia-Gracia, R. El-Ganainy, D. N. Christodoulides, and M. Khajavikhan, Enhanced sensitivity at higher-order exceptional points, Nature (London) **548**, 187 (2017).

[12] Y.-X. Xiao, Z.-Q. Zhang, Z. H. Hang, and C. T. Chan, Anisotropic exceptional points of arbitrary order, Phys. Rev. B **99**, 241403(R) (2019).

[13] S. Wang, B. Hou, W. Lu, Y. Chen, Z. Q. Zhang, and C. T. Chan, Arbitrary order exceptional point induced by photonic spin-orbit interaction in coupled resonators, Nat. Commun. **10**, 832 (2019).

[14] Z. Xiao, H. Li, T. Kottos, and A. Alù, Enhanced Sensing and Nondegraded Thermal Noise Performance Based on PT-Symmetric Electronic Circuits with a Sixth-Order Exceptional Point, Phys. Rev. Lett. **123**, 213901 (2019).

[15] S. M. Zhang, X. Z. Zhang, L. Jin, and Z. Song, High-order exceptional points in supersymmetric arrays, Phys. Rev. A **101**, 033820 (2020).

[16] Y.-X. Xiao, K. Ding, R.-Y. Zhang, Z. H. Hang, and C. T. Chan, Exceptional points make an astroid in non-Hermitian Lieb lattice: Evolution and topological protection, Phys. Rev. B **102**, 245144 (2020).

[17] P. Delplace, T. Yoshida, and Y. Hatsugai, Symmetry-Protected Multifold Exceptional Points and Their Topological Characterization, Phys. Rev. Lett. **127**, 186602 (2021).

[18] I. Mandal and E. J. Bergholtz, Symmetry and Higher-Order Exceptional Points, Phys. Rev. Lett. **127**, 186601 (2021).

[19] L. Feng, Z. J. Wong, R.-M. Ma, Y. Wang, and X. Zhang, Single-mode laser by parity-time symmetry breaking, Science **346**, 972 (2014).

[20] H. Hodaei, M.-A. Miri, M. Heinrich, D. N. Christodoulides, and M. Khajavikhan, Parity-time– symmetric microring lasers, Science **346**, 975 (2014).

[21] W. Chen, S. K. Ozdemir, G. Zhao, J. Wiersig, and L. Yang, Exceptional points enhance sensing in an optical microcavity, Nature (London) **548**, 192 (2017).

[22] K. Ding, G. Ma, Z. Q. Zhang, and C. T. Chan, Experimental Demonstration of an Anisotropic Exceptional Point, Phys. Rev. Lett. **121**, 085702 (2018).

[23] K. Ding, G. Ma, M. Xiao, Z. Q. Zhang, and C. T. Chan, Emergence, Coalescence, and Topological Properties of Multiple Exceptional Points and their Experimental Realization, Phys. Rev. X **6**, 021007 (2016).

[24] Z. Yang, A. P. Schnyder, J. Hu, and C.-K. Chiu, Fermion Doubling Theorems in Two-Dimensional Non-Hermitian Systems for Fermi Points and Exceptional Points, Phys. Rev. Lett. **126**, 086401 (2021).

[25] H. Shen, B. Zhen, and L. Fu, Topological Band Theory for Non-Hermitian Hamiltonians, Phys. Rev. Lett. **120**, 146402 (2018).

[26] D. Leykam, K. Y. Bliokh, C. Huang, Y. D. Chong, and F. Nori, Edge Modes, Degeneracies, and Topological Numbers in Non-Hermitian Systems, Phys. Rev. Lett. **118**, 040401 (2017).

[27] J. C. Garrison and E. M. Wright, Complex Geometrical Phases for Dissipative Systems, Phys. Lett. A **128**, 177 (1988).

[28] A. A. Mailybaev, O. N. Kirillov, and A. P. Seyranian, Geometric phase around exceptional points, Phys. Rev. A **72**, 014104 (2005).

[29] W. Tang, X. Jiang, K. Ding, Y.-X. Xiao, Z.-Q. Zhang, C. T. Chan, and G. Ma, Exceptional nexus with a hybrid topological invariant, Science **370**, 1077 (2020).

[30] K. Kawabata, T. Bessho, and M. Sato, Classification of Exceptional Points and Non-Hermitian Topological Semimetals, Phys. Rev. Lett. **123**, 066405 (2019).

[31] H. Hu and E. Zhao, Knots and Non-Hermitian Bloch Bands, Phys. Rev. Lett. **126**, 010401 (2021).

[32] H. Hu, S. Sun, and S. Chen, Knot topology of exceptional point and non-Hermitian no-go theorem, Phys. Rev. Res. **4**, L022064 (2022).

[33] K. Wang, A. Dutt, C. C. Wojcik, and S. Fan, Topological complex-energy braiding of non-Hermitian bands, Nature (London) **598**, 59 (2021).

[34] G. Demange and E.-M. Graefe, Signatures of three coalescing eigenfunctions, J. Phys. A: Math. Theor. **45**, 025303 (2012).

[35] L. Jin, H. C. Wu, B.-B. Wei, and Z. Song, Hybrid exceptional point created from type-III Dirac point, Phys. Rev. B **101**, 045130 (2020).

[36] H. Jing, Ş. K. Özdemir, H. Lü, and F. Nori, High-order exceptional points in optomechanics, Sci. Rep. **7**, 3386 (2017).

[37] C. Zeng, Y. Sun, G. Li, Y. Li, H. Jiang, Y. Yang, and H. Chen, Enhanced sensitivity at high-order exceptional points in a passive wireless sensing system, Opt. Express **27**, 27562 (2019).

[38] Q. Zhong, J. Kou, Ş. K. Özdemir, and R. El-Ganainy, Hierarchical Construction of Higher-Order Exceptional Points, Phys. Rev. Lett. **125**, 203602 (2020).

[39] Y. Wu, P. Zhou, T. Li, W. Wan, and Y. Zou, High-order exceptional point-based optical sensor, Opt. Express **29**, 6080 (2021).

[40] T. E. Lee, Anomalous Edge State in a Non-Hermitian Lattice, Phys. Rev. Lett. **116**, 133903 (2016).

[41] S. Yao and Z. Wang, Edge States and Topological Invariants of Non-Hermitian Systems, Phys. Rev. Lett. **121**, 086803 (2018).

[42] F. K. Kunst, E. Edvardsson, J. C. Budich, and E. J. Bergholtz, Biorthogonal Bulk-Boundary Correspondence in Non-Hermitian Systems, Phys. Rev. Lett. **121**, 026808 (2018).

[43] K. Yokomizo and S. Murakami, Non-Bloch Band Theory of Non-Hermitian Systems, Phys. Rev. Lett. **123**, 066404 (2019).

[44] E. J. Bergholtz, J. C. Budich, and F. K. Kunst, Exceptional topology of non-Hermitian systems, Rev. Mod. Phys. **93**, 015005 (2021).

[45] N. Okuma, K. Kawabata, K. Shiozaki, and M. Sato, Topological Origin of Non-Hermitian Skin Effects, Phys. Rev. Lett. **124**, 086801 (2020).

[46] K. Zhang, Z. Yang, and C. Fang, Correspondence Between Winding Numbers and Skin Modes in Non-Hermitian Systems, Phys. Rev. Lett. **125**, 126402 (2020).

[47] N. Hatano and D. R. Nelson, Localization transitions in non-Hermitian quantum mechanics, Phys. Rev. Lett. **77**, 570 (1996).

[48] Y.-X. Xiao and C. T. Chan, Topology in non-Hermitian Chern insulators with skin effect, Phys. Rev. B **105**, 075128 (2022).

[49] See Supplemental Material at http://link.aps.org/supplemental/10.1103/PhysRevB.108.115427 for the details of circuit implementation, splitting rules, symmetries and exceptional ellipses, which includes Refs. [11,14,16,24,29,50–60].

[50] C. D. Meyer, *Matrix Analysis and Applied Linear Algebra* (SIAM, Philadelphia, PA, 2000).

[51] A. Mostafazadeh, Pseudo-Hermiticity versus PT-symmetry. II. A complete characterization of non-Hermitian Hamiltonians with a real spectrum, J. Math. Phys. **43**, 2814 (2002).

[52] B. Zhen, C. W. Hsu, Y. Igarashi, L. Lu, I. Kaminer, A. Pick, S.-L. Chua, J. D. Joannopoulos, and M. Soljacic, Spawning rings of exceptional points out of Dirac cones, Nature (London) **525**, 354 (2015).

[53] A. Cerjan, S. Huang, M. Wang, K. P. Chen, Y. Chong, and M. C. Rechtsman, Experimental realization of a Weyl exceptional ring, Nat. Photon. **13**, 623 (2019).

[54] T. Yoshida, R. Peters, N. Kawakami, and Y. Hatsugai, Symmetry-protected exceptional rings in two-dimensional correlated systems with chiral symmetry, Phys. Rev. B **99**, 121101(R) (2019).

[55] T. Liu, J. J. He, Z. Yang, and F. Nori, Higher-Order Weyl-Exceptional-Ring Semimetals, Phys. Rev. Lett. **127**, 196801 (2021).

[56] G. Xu, W. Li, X. Zhou, H. Li, Y. Li, S. Fan, S. Zhang, D. N. Christodoulides, and C.-W. Qiu, Observation of Weyl exceptional rings in thermal diffusion, Proc. Natl. Acad. Sci. USA **119**, e2110018119 (2022).

[57] W. Tang, K. Ding, and G. Ma, Direct Measurement of Topological Properties of an Exceptional Parabola, Phys. Rev. Lett. **127**, 034301 (2021).

[58] H. Zhou, J. Y. Lee, S. Liu, and B. Zhen, Exceptional surfaces in PT-symmetric non-Hermitian photonic systems, Optica **6**, 190 (2019).

[59] X. Zhang, K. Ding, X. Zhou, J. Xu, and D. Jin, Experimental Observation of an Exceptional Surface in Synthetic Dimensions with Magnon Polaritons, Phys. Rev. Lett. **123**, 237202 (2019).

[60] J. J. Sakurai, *Modern Quantum Mechanics* (Addison-Wesley Publishing, Reading, MA, 1994).

[61] C. H. Lee, S. Imhof, C. Berger, F. Bayer, J. Brehm, L. W. Molenkamp, T. Kiessling, and R. Thomale, Topolectrical circuits, Commun. Phys. **1**, 39 (2018).

[62] T. Hofmann, T. Helbig, C. H. Lee, M. Greiter, and R. Thomale, Chiral Voltage Propagation and Calibration in a Topolectrical Chern Circuit, Phys. Rev. Lett. **122**, 247702 (2019).

[63] T. Helbig, T. Hofmann, S. Imhof, M. Abdelghany, T. Kiessling, L. W. Molenkamp, C. H. Lee, A. Szameit, M. Greiter, and R. Thomale, Generalized bulk– boundary correspondence in non-Hermitian topolectrical circuits, Nat. Phys. **16**, 747 (2020).